ATMOSPHERIC SCIENCE

Superoxide formation upon photochemical aging of secondary organic aerosols derived from biomass burning precursors

Lena Gerritz, Meredith Schervish, Pascale S. J. Lakey, Sergey A. Nizkorodov, Manabu Shiraiwa*

Photochemical oxidation in the aqueous phase is critical for chemical evolution of secondary organic aerosols (SOA), but it represents one of the most uncertain processes in aerosols and clouds. Here, we show that photoirradiation of SOA derived from biomass burning precursors leads to substantial formation of superoxide. The combination of laboratory measurements and kinetic modeling reveals that superoxide generation is driven by photosensitization reactions in aromatic SOA, while the dominant source of superoxide in biogenic SOA is photoinduced decomposition of carbonyls with minor contributions from peroxide decomposition. These processes serve as a substantial source of reactive oxygen species (ROS) including hydrogen peroxide and hydroxyl radical in cloud droplets and deliquesced particles, competing with traditional sources such as uptake from the gas phase. This previously unrecognized source of ROS will enhance the impact of aqueous-phase processing on composition and properties of aerosols and clouds.

INTRODUCTION

Organic aerosols play a central role in air quality, climate, and human health, and it is crucial to understand their composition and properties to elucidate the full range of their environmental impacts (*1*, *2*). An increasingly important source of organic aerosols in the atmosphere is biomass burning as wildfires become more frequent and intense upon global environmental change (*3*, *4*). Biomass burning emits massive amounts of particulate matter and volatile organic compounds (VOCs) (*5*, *6*). These VOCs can be oxidized during atmospheric transport of the smoke to form biomass burning secondary organic aerosols (BBSOA) that contribute substantially to total particulate matter mass (*7*–*9*). The composition of VOCs is complex depending on environmental factors such as the conditions of burning and fuel types (*3*, *7*, *10*). These VOCs include monoterpenes and terpenoids, which have been thoroughly studied as a source of biogenic secondary organic aerosol (SOA) (*2*, *11*). Recent studies have identified other major classes of VOCs including aromatic and furan derivatives as important contributors to BBSOA (*8*, *12*–*15*), although they are less studied.

The formed BBSOA is subject to atmospheric aging via photochemistry and aqueous-phase chemistry, leading to the chemical transformation of organic compounds and formation of aqueous SOA (*16*). Condensed-phase photochemical processes are known to promote aging of organic particles as much, if not more, than aging by reactions with gaseous $^{\bullet}OH$ (*17*). These aging processes modulate chemical composition and aerosol properties including hygroscopicity, optical properties, and toxicity (*11*, *18*). Previous studies have shown that direct photolysis of biogenic SOA can lead to particle mass loss via decomposition of peroxides and carbonyls (*19*–*21*), whereas photosensitized reactions in aromatic SOA can lead to aqueous SOA formation (*22*–*24*).

Aqueous-phase oxidation processes are driven by reactive oxygen species (ROS) including hydroxyl radical ($^{\bullet}OH$), superoxide ($HO_2^{\bullet}/O_2^{-\bullet}$), singlet oxygen ($^1O_2$), hydrogen peroxide ($H_2O_2$), and oxygen-centered organic radicals (*1*). A light-driven burst of $^{\bullet}OH$ radicals was observed to dominate oxidation chemistry in newly activated cloud droplets (*25*). SOA can produce $^{\bullet}OH$ from the decomposition of organic hydroperoxides under dark conditions (*26*, *27*), which can be enhanced by the presence of transition metals or photolysis (*28*–*31*). In our recent work, we observed substantial ROS formation upon photoirradiation of SOA derived from isoprene and terpenes driven by decomposition of peroxides and carbonyls (*32*). Photosensitizers, which are often contained in aromatic SOA, can also generate ROS (*33*–*36*), increasing the aqueous oxidant concentrations and further altering the particle composition and oxidation processes. In addition to the competing photochemical pathways, mechanistic understanding of aqueous photochemistry is further complicated by the central role of free radical intermediates that evade most analytical methods. The chemical mechanism and kinetics of ROS formation upon complex photochemical interplay of BBSOA are hardly explored and poorly understood. Better assessment of BBSOA impacts on atmospheric chemistry and climate requires molecular-level understanding of ROS multiphase chemistry.

In this work, we observed enhanced superoxide formation upon photoirradiation of a wide range of BBSOA derived from monoterpenes (α-pinene, α-terpineol, and β-ocimene), mono-aromatics (phenol, styrene, and guaiacyl acetone), furfural, and naphthalene. We applied an in situ ultraviolet-visible (UV-Vis) irradiation system with electron paramagnetic resonance (EPR) spectroscopy to measure the radical formation, and we identified the trapped radicals using high-resolution mass spectrometry. The application of kinetic modeling in combination with total peroxide measurements revealed relative contributions of radical formation pathways including direct photosensitization, carbonyl photolysis, and peroxide decomposition. The superoxide formation leads to substantial formation of H_2O_2, outcompeting known processes and measured concentrations of H_2O_2.

RESULTS AND DISCUSSION

ROS formation

Figure 1 shows the time evolution of superoxide ($HO_2^{\bullet}/O_2^{-\bullet}$) as trapped by 5-*tert*-butoxycarbonyl-5-methyl-1-pyrroline-*N*-oxide

Department of Chemistry, University of California, Irvine, Irvine, CA, USA.
*Corresponding author. Email: m.shiraiwa@uci.edu

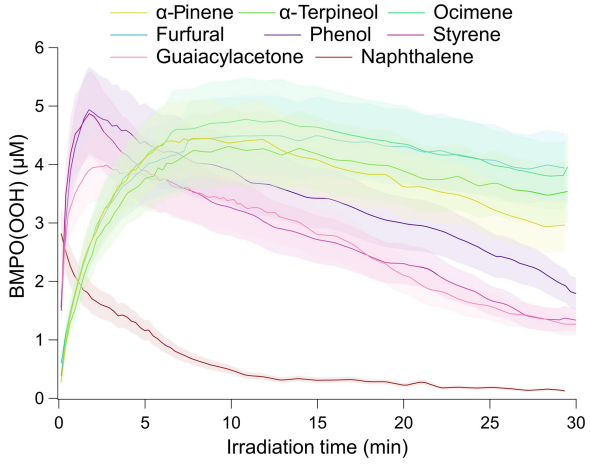

Fig. 1. Superoxide formation kinetics in different types of BBSOA. Formation kinetics of BMPO(OOH) during the in situ irradiation of seven types of SOA as detected by EPR starting 7 s after irradiation begins. Before irradiation, BMPO(OOH) was close to the detection limit (~0.2 μM) except for naphthalene SOA (~0.7 μM) (see fig. S1). The shading represents 15% uncertainty (an upper bound for one SD of replicate measurements).

(BMPO) upon in situ irradiation of water extracts of BBSOA derived from monoterpenes, aromatics, and furfural. We observed substantial superoxide formation for all types of SOA, reaching maximum concentrations of ~4 to 5 μM, along with lower concentrations of other radicals shown in fig. S4. This corresponds to superoxide yields (mole superoxide per mole SOA) of 0.4 to 0.5%. The observed concentrations are much higher than those under dark conditions (fig. S1), which was close to detection limit (~0.2 μM) for most types of SOA. Note that naphthalene SOA showed noticeable dark superoxide formation (~0.7 μM) due to redox reactions of semiquinones and environmentally persistent free radicals, consistent with previous studies (*37*–*39*). Thus, photolysis enhanced the superoxide formation by a factor of 4 to 25. Maximum superoxide concentrations were reached shortly after irradiation by aromatic SOA, whereas it took ~10 min for monoterpene and furfural SOA. The distinction in superoxide formation kinetics indicates that the dominant mechanism of superoxide formation is different, as discussed in detail in the "Kinetic modeling" section.

The similar maximum concentrations of BMPO(OOH) among different types of SOA imply that superoxide formation is limited by a common process. We hypothesized that the dissolved oxygen may undergo depletion in the closed system and the amount of dissolved oxygen may limit subsequent superoxide formation as molecular oxygen is most likely a major precursor of superoxide. Additional experiments with different concentrations of α-pinene and phenol SOA (fig. S2A), as well as pure compounds including cumene hydroperoxide and pinonic acid (fig. S2B), resulted in similar maximum BMPO(OOH) concentrations. We also measured BMPO(OOH) formation by α-pinene SOA under different temperatures and observed that BMPO(OOH) formation is larger at lower temperatures and smaller at higher temperatures, correlating very well with dissolved oxygen concentration as calculated using the Henry's law constant (fig. S3). This indicates that dissolved oxygen plays a critical role in the formation of superoxide. The lower maximum superoxide concentration by naphthalene SOA may be caused by higher scavenging of superoxide by redox-active compounds such as semiquinones contained in naphthalene SOA (*40*).

In addition to the enhanced superoxide formation upon irradiation, we also observed the formation of carbon- and oxygen-centered organic radicals. As shown in the deconvoluted EPR spectra and time evolution of radical formation by SOA derived from α-pinene, furfural, and phenol (fig. S4), the monoterpene SOA produced more organic radicals than the aromatic SOA, consistent with previous results comparing terpene and toluene SOA (*32*). Using high-resolution mass spectrometry, we identified major organic radicals produced during irradiation of furfural and phenol SOA (figs. S5 to S8). The major organic radicals trapped for furfural SOA are $CHO^{\bullet}$ and $CHO_2^{\bullet}$ radicals, identified on the basis of their retention time and fragmentation mass spectra (figs. S9 to S11) (*41*), likely products of aldehyde and ester photolysis (*42*, *43*). Sample photolysis pathways yielding $CHO^{\bullet}$ and $CHO_2^{\bullet}$ are shown in fig. S12 for $C_4H_6O_5$, one of the ions identified by mass spectrometry that decreased the most after irradiation. Aldehyde photolysis can form $HO_2^{\bullet}$, as previously described for α-pinene SOA (*32*). Ester photolysis can lead to the formation of α-hydroxy radicals, which can react with O_2 to form α-hydroxy peroxy radicals that may decompose to produce $HO_2^{\bullet}$ (*39*, *44*). While the organic radicals were formed less in phenol SOA, the most prominent product is the $C_6H_5O_3^{\bullet}$ radical (fig. S6), which is the expected product for the photosensitization reaction between $C_6H_6O_3$ (trihydroxybenzene, known product of phenol oxidation) and dissolved oxygen (*45*). The organic radicals identified using mass spectrometry indicate the occurrence of ester and carbonyl photolysis in furfural SOA and the photosensitization reactions in phenol SOA.

We carried out separate experiments to measure H_2O_2 in the absence of a spin trap before and after irradiation of SOA for 10 min. As shown in Fig. 2, before irradiation, the H_2O_2 yields are lower at 0.26 and 0.30% for α-terpineol and α-pinene SOA, respectively. They are higher at 0.80 and 1.1% for furfural and ocimene SOA, respectively, and they are in the range of 0.7 to 1.0% for aromatic SOA. These values are comparable to H_2O_2 yields previously reported for monoterpene and aromatic SOA (*26*, *39*, *46*, *47*).

After irradiation, the H_2O_2 yields become higher for all types of SOA, indicating that photolysis can induce H_2O_2 formation. They

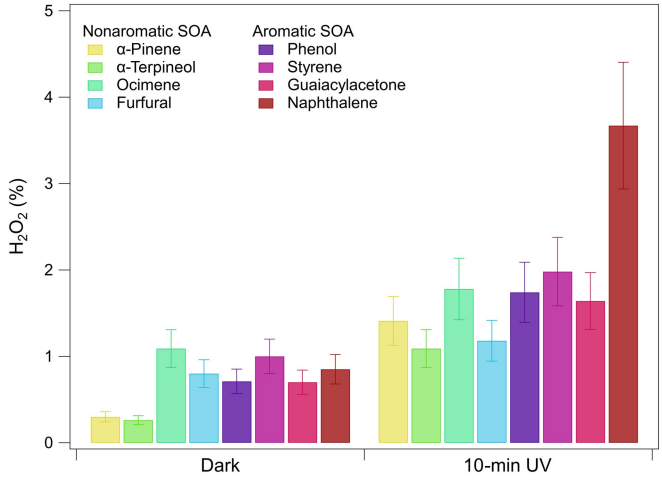

Fig. 2. H_2O_2 molar yields before and after irradiation. Measured molar H_2O_2 yields for each type of SOA before and after irradiation. Error bars represent 20% uncertainty (an upper bound for one SD of replicate measurements).

increased to the range of 1.2 to 1.8% for nonaromatic SOA, representing an increase by a factor of ~1.5 to 4 compared with dark conditions. For mono-aromatic SOA, H_2O_2 yields approximately doubled to be 1.6 to 2.0%. Naphthalene SOA produced the most H_2O_2 after irradiation with 3.7% yield, representing an increase by about a factor of 5 from dark conditions. These results confirm that irradiation leads to enhancement in aqueous H_2O_2 for a variety of types of SOA, supporting that photochemistry is one of the factors contributing to the elevated concentrations of H_2O_2 observed in ambient aerosols (*48*).

Kinetics and chemical mechanism

To elucidate the reaction kinetics and mechanism, we developed a kinetic box model to simulate the measured temporal evolution of superoxide and H_2O_2. The model considers three potential pathways for ROS formation: direct photosensitization, carbonyl photolysis, and peroxide photolysis, as shown in Fig. 3 and table S1. Some types of SOA, especially aromatic SOA, contain photosensitizing compounds that can absorb UV to become a triplet state, which can react with dissolved oxygen to form superoxide (*35*, *40*, *49*, *50*). Carbonyl species can undergo Norrish type I photolysis to produce ketyl or formyl radicals that react with oxygen to produce $HO_2^{\bullet}$ (*51*). Photolysis of organic hydroperoxides can generate $^{\bullet}OH$, which can oxidize primary or secondary alcohols and subsequent reaction with dissolved oxygen leads to the formation of α-hydroxy peroxyl radical, which can decompose to form $HO_2^{\bullet}$ (*32*, *39*). The self-reactions of $O_2^{-\bullet}/HO_2^{\bullet}$ lead to the formation of H_2O_2. Other reactions include radical trapping by BMPO, ROS coupling reactions,

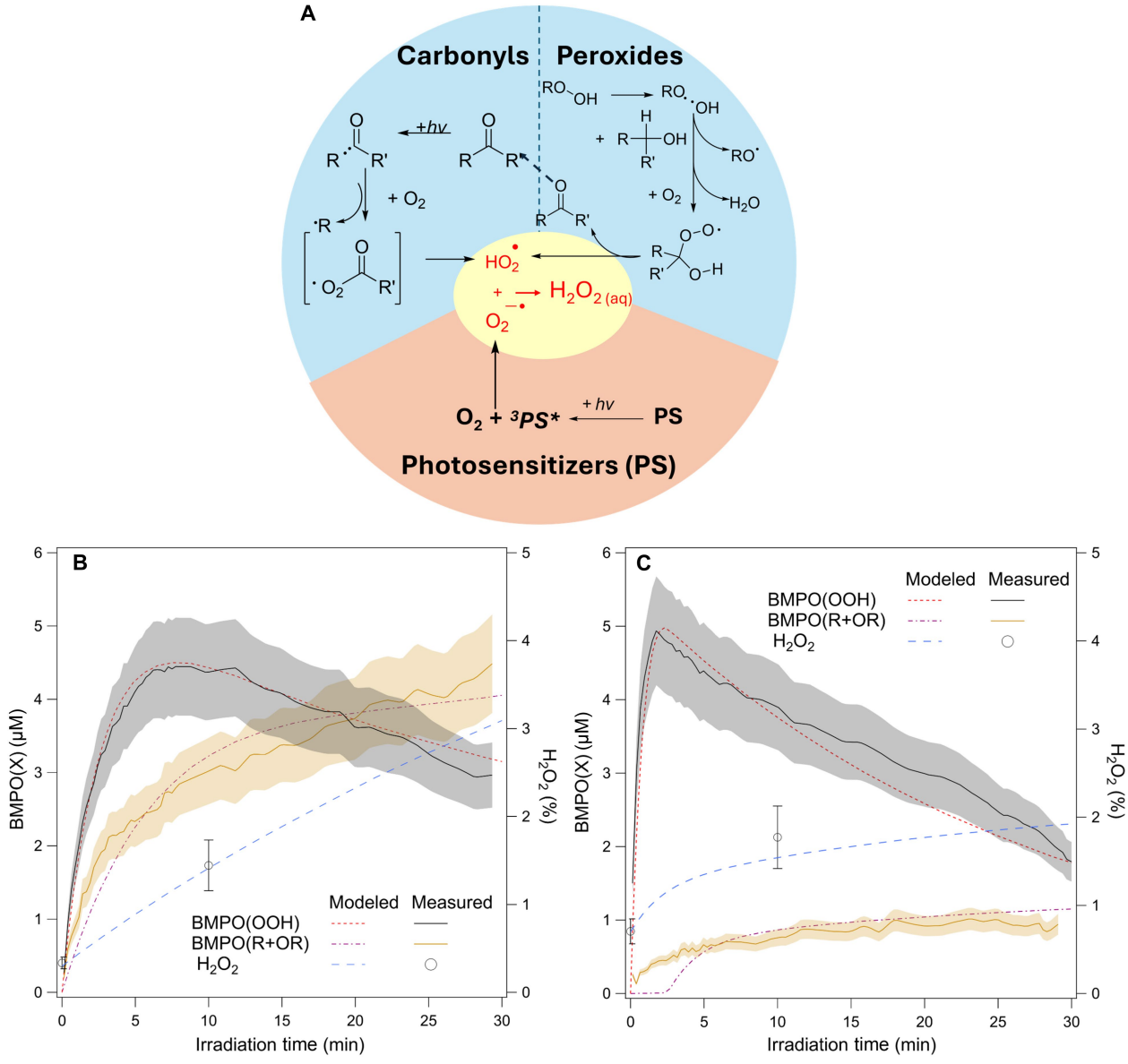

Fig. 3. Modeled mechanisms of ROS formation. (**A**) Graphical summary of the photochemical processes included in the kinetic model to explain the formation of superoxide. (**B**) Measured (solid lines and marker) and best-fit model output (dashed lines) for BMPO(OOH), BMPO(R+OR), and H_2O_2 formation from α-pinene and (**C**) phenol SOA. Shading represents 15% uncertainty for EPR measurements, and error bars represent 20% uncertainty for the H_2O_2 measurements.

and radical termination reactions, as listed in table S1. We simulated temporal evolution of light-driven ROS formation by α-pinene and phenol SOA, as representative cases for monoterpene and monoaromatic SOA, respectively. The rate coefficients of known reactions were obtained from literature values, the dissolved oxygen concentrations were fixed on the basis of Henry's law, and the molar fractions of organic peroxides are fixed with measurements for α-pinene SOA (fig. S13) and estimated for phenol SOA as described in the Supplementary Materials. The unknown rate coefficients and molar fractions of photosensitizers, carbonyls, and alcohols contained in SOA were determined using the Monte Carlo genetic algorithm (MCGA) to reproduce experimental data and constrained based on previous literature cited in table S1 (*52*).

As shown in Fig. 3 (B and C), the model successfully reproduced the formation of BMPO(OOH), total organic radicals [BMPO(R+OR)], and H_2O_2 for both α-pinene and phenol SOA. The model captures distinct differences in the kinetics of radical formation: a fast increase of superoxide and substantial formation of organic radicals in α-pinene SOA and almost instantaneous production of superoxide and gradual increase of organic radicals in phenol SOA. For α-pinene SOA, the model attributes most of the superoxide formation to photolysis of carbonyls; without carbonyl photolysis, the kinetics of substantial formation of organic radicals cannot be captured well (fig. S14). In contrast, the superoxide formation in phenol SOA is solely driven by photosensitized reactions with very fast excitation of photosensitizer molecules and electron transfer to dissolved oxygen (fig. S15). This leads to rapid depletion of dissolved oxygen, leading to saturation and decrease of BMPO(OOH) (fig. S16). Note that we exclude photobleaching of photosensitizer molecules as a reason for decrease of superoxide formation as UV-Vis absorption spectra of α-pinene SOA and phenol SOA remain mostly unchanged after photoirradiation (figs. S20 and S21). For both SOA systems, peroxide pathways are found to be minor due to low measured concentrations of organic peroxides. The model predicts gradual accumulation of H_2O_2 as generated by HO_x self-reactions. The measurements showed minimal dependence of H_2O_2 formation on SOA concentration, which is captured well by the model (fig. S17). These results suggest the importance of photosensitizer processes in aromatic SOA and carbonyl photolysis in monoterpene SOA.

Implications

To evaluate the impact of photolysis on ROS concentrations in aqueous BBSOA droplets under ambient conditions, we conducted model simulations using constrained parameters (table S1) in the absence of BMPO. To reflect the open system under ambient conditions, we used a constant dissolved oxygen concentration based on Henry's law. The solid lines in Fig. 4A show the predicted concentrations of H_2O_2, superoxide ($HO_2^{\bullet}/O_2^{-\bullet}$), and $^{\bullet}OH$ produced during aqueous irradiation of α-pinene and phenol SOA at different concentrations ranging from dilute cloud and fog droplets to deliquesced ambient particles. The predicted concentrations are compared with previous measurements and model calculations (*34*, *53*–*56*). The shaded regions correspond to the concentrations calculated using Henry's law using previously reported ambient mixing ratios of 0.01– to 6–part-per-billion (ppb) H_2O_2 and 0.03– to 43–part-per-thousand (ppt) $HO_2^{\bullet}$. In addition, we also calculated the photochemical production rates of each oxidant, as shown in lines and shaded areas in Fig. 4B. These values are comparable to or higher than most field observations (*31*, *35*, *36*, *40*, *54*, *57*–*61*), strongly

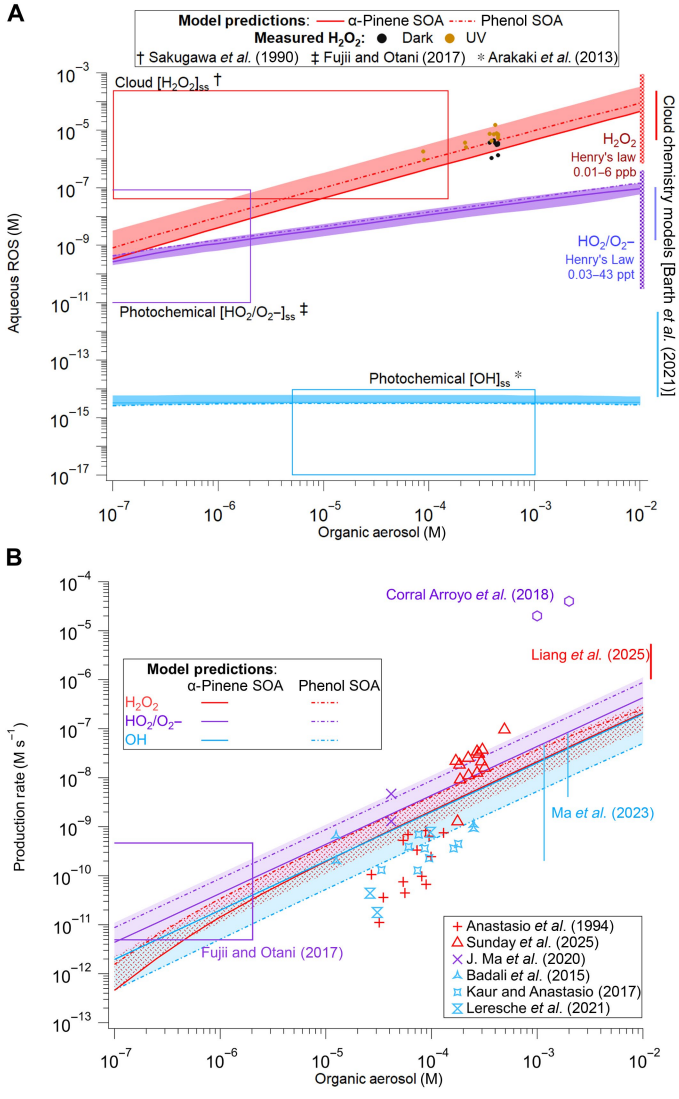

Fig. 4. Predicted ROS concentrations and production rates. (**A**) Concentrations and (**B**) production rates of H_2O_2 (red), superoxide ($HO_2^{\bullet}/O_2^{-\bullet}$) (purple), and $^{\bullet}OH$ (blue) in aqueous droplets as a function of organic aerosol concentration. The solid and dashed lines represent the predicted ROS in α-pinene and phenol SOA, respectively, after 1 h of equivalent aging in Los Angeles, whereas the shaded regions show the range of ROS during 30 h of equivalent aging (see the Supplementary Materials for calculations). In (A), the black and brown markers represent measured H_2O_2 concentrations in this study, and the boxes represent previously measured concentrations for H_2O_2 (*53*) and $^{\bullet}OH$ (*34*, *55*) in ambient cloud or fog droplets and for $HO_2^{\bullet}$ (*54*) in natural water. The checkered bars in the right axis correspond to the concentrations calculated using Henry's law with previously reported ranges for ambient mixing ratios (*76*), and the bars show the range previously predicted by various cloud chemistry models (*56*). The markers in (B) show production rates for H_2O_2 (*36*, *58*), $HO_2^{\bullet}/O_2^{-\bullet}$ (*35*, *40*, *54*), and $^{\bullet}OH$ (*31*, *60*, *61*) from literature. The organic aerosol concentrations were estimated, when possible, from reported dissolved organic carbon concentrations by assuming an average of 10 carbons per molecule. The boxes comparing the $HO_2^{\bullet}/O_2^{-\bullet}$ concentration and production rate measured by Fujii and Otani (*54*) use organic aerosol concentrations estimated for HULIS molar mass ranging from 500 to 10,000 (*77*).

implying that photoenhanced superoxide formation in SOA can compete with other ROS formation pathways.

All the predicted oxidant concentrations and production rates are within the ranges of previous measurements and model estimates, indicating that this aqueous photochemistry and superoxide formation in BBSOA produces atmospherically relevant concentrations of oxidants in the aqueous phase. At lower organic aerosol concentrations, the model-predicted H_2O_2 concentration is significantly lower than the range calculated using Henry's law, indicating that photochemical formation is negligible relative to partitioning of H_2O_2 from the gas phase. Contrastingly, at high organic aerosol concentrations, the predicted H_2O_2 and $HO_2^{\bullet}$ concentrations and production rates are comparable with measurements and within the range of previous model calculations. $^{\bullet}OH$ can be produced by photolysis of generated H_2O_2 and organic hydroperoxides and ROS coupling reactions; the predicted $^{\bullet}OH$ concentrations are in the upper range of ambient measurements in cloud or fog droplets. Note that the mass transfer rate of gas-particle partitioning is rapid, and it is reasonable to assume that gas-particle equilibrium is established with photoirradiation shifting the steady-state concentrations; the produced ROS may participate in reactions in the condensed phase or can be transported to the gas phase (see analysis of mass transfer rates in the Supplementary Materials). These results demonstrate that photochemistry of BBSOA can significantly enhance the concentrations of ROS including H_2O_2, $HO_2^{\bullet}$, and $^{\bullet}OH$ in deliquesced particles and aqueous droplets with high organic aerosol concentrations. The photoproduction of H_2O_2 and $HO_2^{\bullet}$ is likely an important pathway especially in high NO_x environments where their gas-phase mixing ratios are often low (*53*, *62*). In addition, the predicted aqueous-phase H_2O_2 concentration at high organic aerosol concentrations would correspond to a Henry's law equilibrium gas-phase concentration of 1 ppb, which is consistent with the gas-phase concentration measured by a recent study finding that photosensitization reactions of particulate matter produce H_2O_2 in the gas phase (*63*). Our work elucidates the previously unidentified mechanism of superoxide formation and subsequent ROS formation that can explain enhanced gas-phase oxidant concentrations during photochemical aging.

While this study focuses on BBSOA, primary-emitted biomass burning aerosols contain high amounts of brown carbon (BrC) and transition metals (*18*, *64*). Light absorption by BrC chromophores can lead to the formation of triplet excited states ($^3C^*$), which can undergo reactions with dissolved oxygen to form singlet oxygen ($^1O_2$) and with dissolved organic carbon to produce H_2O_2 (*34*, *36*, *65*). Aqueous oxidation of dissolved organics can lead to an increase in aerosol mass and alters the physicochemical properties of aerosols such as optical properties and cloud activation properties (*66*). Recent studies have demonstrated that these photooxidants generated via photosensitization can be significant intermediates for secondary sulfate from oxidation of sulfur(IV) (*67*). In addition, ROS can catalyze aqueous aging via radical chain reactions, promoting the formation of oxidation products (fig. S18). Such aqueous oxidation of organic compounds and sulfur(IV) may be promoted in the presence of transition metals via Fenton-like reactions and metal-catalyzed reactions (*29*, *68*). The presence of transition metals will also affect both source and sink of ROS; in addition, some organic compounds may form metal complexes, further complicating ROS processes (*69*).

ROS also have important implications for toxicity and health impacts of aerosols. Light-driven formation of H_2O_2 may increase particle toxicity as ROS are known to induce oxidative stress, which is associated with various negative health outcomes (*1*, *70*). Previous studies have shown that photoirradiation increased oxidative potential of BBOA (*71*) and photochemically aged SOA increased toxicity effects (*72*), although the overall impact of aging on toxicity requires more investigation. ROS plays a critical role in the physical and chemical transformation of atmospheric aerosols with important implications for health and climate. This work fills a critical gap in the mechanistic understanding of aqueous-phase ROS formation upon photochemical aging of BBSOA. These findings provide useful insights to improve representation of photochemical aging of aerosols and oxidant budgets in atmospheric aerosol models.

MATERIALS AND METHODS

Environmental chamber sample generation

SOA samples were generated via the $^{\bullet}OH$ oxidation of precursors in a 5-m^3 Teflon reaction chamber humidified to ~30%, as previously described (*32*). Briefly, the VOC precursor and hydrogen peroxide (Thermo Fisher Scientific, 30% in water) were injected into the chamber by evaporation into a clean air flow at ~70°C. An $^{\bullet}OH$ steady-state concentration of ~10^7 cm^{-3} was generated via photolysis of H_2O_2 by UV-B lamps centered around 310 nm. α-Pinene, α-terpineol, β-ocimene, phenol, and naphthalene SOA was generated from ~2 parts per million (ppm) of H_2O_2 and ~200 ppb of the precursor, whereas styrene, guaiacyl acetone, and furfural SOA particles were generated from 4 ppm of H_2O_2 and ~400 ppb of precursor due to lower SOA yields. No NO_x was intentionally added to the chamber, and total NO_y levels remained below 5 ppb during all experiments. Following 2 h of irradiation, all SOA particles were collected onto PTFE filters (Millipore, 0.2 μM pore size) at a flow rate of ~22 SLM for 2 to 3 h. The particle size distribution was measured using a TSI classifier model 3080 SMPS, and the collected SOA mass was estimated assuming 100% filter collection efficiency and aerosol particle density of 1.20 g cm^{-3}. For offline analysis, the SOA was dissolved in Milli-Q water via vortex extraction for 7 min to produce aqueous SOA samples with effective 1 to 2 mM concentrations, assuming an average molar mass of 200 g mol^{-1}.

Free radical detection

Free radicals were measured using a continuous-wave EPR spectrometer (Bruker, Germany), as previously described (*73*). To trap free radicals, >10 mM of spin-trapping agent BMPO (Cayman Chemicals) was added to the aqueous SOA solution. Aliquots (50 μl) of the mixture were then added into a 50-μl capillary tube (VWR) and sealed before being placed in the EPR resonator for analysis. Before irradiation, the EPR measurements were conducted for each sample to determine radical formation under dark conditions. The samples were then exposed to in situ irradiation (ER203UV, Bruker, Germany) covering the range of 280 to 600 nm from a 100-W Hg lamp with a 300-nm cutoff filter, and radical formation was measured over the course of irradiation. The operating parameters for EPR measurements were as follows: a center field of 3515.0 G, a sweep width of 100.0 G, a receiver gain of 30 dB, a modulation amplitude of 1.0 G, a scan number of 1 to 5, attenuation of 12 dB, a microwave power of 12.6 mW, a modulation frequency of 100 kHz, a microwave frequency of 9.84 GHz, and a conversion time and time constant of 5.12 ms. After obtaining the EPR spectra, the SpinFit and SpinCount methods embedded in the Bruker Xenon software

were applied to deconvolute spectra to identify different types of radicals ($HO_2^{\bullet}/O_2^{-\bullet}$, $^{\bullet}OH$, and carbon- and oxygen-centered radicals; see fig. S4) and to quantify BMPO-radical adducts at each time point, respectively.

High-resolution mass spectrometry

Chemical analysis of the samples was conducted as previously described (*32*). Briefly, the filter was extracted in Milli-Q water and divided into four samples for the following conditions: nonirradiated without BMPO, irradiated without BMPO, nonirradiated with 10 mM BMPO, and irradiated with 10 mM BMPO. Irradiated samples were exposed to the same lamp as described in the "Free radical detection" section for 60 min. The aqueous samples were diluted to a final volume of ~0.4 g liter^{-1} BMPO in 50/50 v/v water/acetonitrile (Thermo Fisher Scientific). The mass spectrometry performed using the methods described for BMPO adduct identification by Gerritz *et al.* (*41*). The instrument was a Thermo Scientific Vanquish Horizon ultraperformance liquid chromatography system coupled to a Thermo Scientific Q Exactive Plus Orbitrap HR-MS with a heated electrospray ionization source. The data were processed using MZmine version 3.9 to resolve species and remove contaminants based on chromatographic features, as described by Schmid *et al.* (*74*). The mass spectra were integrated between 1.3- and 14-min range of retention times to obtain integrated mass spectra used in the analysis. Peaks due to ^{13}C compounds and peaks that appeared in the blank at the same or greater intensity as the sample were also discarded. The peaks were assigned with 0.001 mass/charge ratio accuracy to formulas [$C_xH_yO_zN_{0-2}$].

H_2O_2 assay

The H_2O_2 content for α-pinene, furfural, and phenol SOA was quantified using a fluorometric hydrogen peroxide assay kit (MAK165, Sigma-Aldrich) following the procedure in the provided technical bulletin. All chemicals used were provided in the kit. A working solution was made using the company recommended ratio of 50 μl of red peroxidase substrate stock, 200 μl of peroxidase stock (20 U/ml), and 4.75 ml of assay buffer. Calibration standards were prepared using the 3% H_2O_2 diluted into assay buffer to make a calibration from 0.530 μM. The SOA filters were extracted in Milli-Q water and divided up into dark samples and irradiated samples that were exposed to the same lamp described in the "Free radical detection" section for 10 min. The SOA samples were diluted using assay buffer to obtain a final concentration of ~100 μg/ml. Aliquots (50 μl) of the calibration standards and samples were added in triplicate to a 96-well plate followed by the addition of 50 μl of working solution to each well. The plate was then covered with tinfoil to minimize exposure to light and left to develop for 20 min. The fluorescence was measured using an excitation wavelength of 520 nm and emission wavelength range of 580 to 640 using the Promega GloMax Discover microplate reader. Control samples were also measured for SOA using the assay buffer in place of the working solution, and no fluorescence was detected. Unlike the EPR measurements, these systems were open to air and should not be depleted in dissolved oxygen offering quantitative insight into the formation of ROS from different processes. The results are presented as molar yield assuming an average SOA mass of 200 g mol^{-1}.

Kinetic modeling

We modeled the formation of BMPO(OOH), BMPO(R), and H_2O_2 during the irradiation of α-pinene and phenol SOA extracts using rate equations derived from the reaction mechanism presented in table S1. Three mechanisms for production of $HO_2^{\bullet}/O_2^{-\bullet}$ are implemented. The first involves a single-electron transfer between a photosensitized species and dissolved oxygen, as proposed for dissolved organic matter by Zhang *et al.* (*50*), represented by reactions R1-R3. The second mechanism (R6-R7) produces $HO_2^{\bullet}$ from carbonyl photolysis (*51*). We also consider the photolysis of peroxides (R10-R14) that produces $^{\bullet}OH$ that reacts with secondary alcohols to produce $HO_2^{\bullet}$, using rate constants adapted from Wei *et al.* (*39*). The rate constants for reactions 1 to 10 were determined using the MCGA to fit the EPR signals for BMPO(OOH), as previously described (*52*, *73*). The range for the rate constants was set on the basis of literature values, when available, but set with an initial range of ~4 orders of magnitude to allow sufficient flexibility. The best-fit rate constants for each type of SOA are reported in table S1.

The resulting radicals can be trapped by BMPO to form stable radical adducts that can be detected via EPR (R15-R20). The rate constants for reactions 15, 17, and 18 were fixed on the basis of previous measurements, but k_{16} was varied to account for variations in the total radical concentration that affect the decomposition rate of BMPO adducts through disproportionation reactions (*41*). The organic radicals BMPO(R+OR) were grouped together as BMPO(R) for the model because the location of the radical is influenced by the stability of the molecule, which cannot be predicted using generalized reaction mechanisms. The rate constants for the formation and decomposition of organic radical adducts [BMPO(R), R19 and R20] were also fit using the experimental data to account for variations in radical identity and reactivity. The interconversion of ROS is included (R21-R30) using fixed rate constants at pH 5, as previously described (*39*, *73*). The model includes reactions R31-R34 to account for interconversion between different organic radicals and radical recombination and R35 to account for the aqueous oxidation of SOA by $^{\bullet}OH$. The rate constant for R30 was fixed, whereas the rate constants for R31-R33 were varied within narrow bounds based on the rate constants provided by Wei *et al.* (*75*). The initial concentration of BMPO, SOA, dissolved oxygen, H_2O_2, and organic peroxides was fixed on the basis of the experimental data. The fractions of photosensitizers and carbonyls in α-pinene and phenol SOA were estimated in the model based on ranges from literature, described further in the Supplementary Materials.

Supplementary Materials

This PDF file includes:

Figs. S1 to S21
Table S1
References

REFERENCES

1. U. Pöschl, M. Shiraiwa, Multiphase chemistry at the atmosphere–biosphere interface influencing climate and public health in the anthropocene. *Chem. Rev.* **115**, 4440–4475 (2015).
2. M. Shrivastava, C. D. Cappa, J. Fan, A. H. Goldstein, A. B. Guenther, J. L. Jimenez, C. Kuang, A. Laskin, S. T. Martin, N. L. Ng, T. Petaja, J. R. Pierce, P. J. Rasch, P. Roldin, J. H. Seinfeld, J. Shilling, J. N. Smith, J. A. Thornton, R. Volkamer, J. Wang, D. R. Worsnop, R. A. Zaveri, A. Zelenyuk, Q. Zhang, Recent advances in understanding secondary organic aerosol: Implications for global climate forcing. *Rev. Geophys.* **55**, 509–559 (2017).
3. M. O. Andreae, Emission of trace gases and aerosols from biomass burning – An updated assessment. *Atmos. Chem. Phys.* **19**, 8523–8546 (2019).
4. A. L. Westerling, H. G. Hidalgo, D. R. Cayan, T. W. Swetnam, Warming and earlier spring increase western U.S. forest wildfire activity. *Science* **313**, 940–943 (2006).
5. T. C. Bond, S. J. Doherty, D. W. Fahey, P. M. Forster, T. Berntsen, B. J. DeAngelo, M. G. Flanner, S. Ghan, B. Kärcher, D. Koch, S. Kinne, Y. Kondo, P. K. Quinn, M. C. Sarofim,

M. G. Schultz, M. Schulz, C. Venkataraman, H. Zhang, S. Zhang, N. Bellouin, S. K. Guttikunda, P. K. Hopke, M. Z. Jacobson, J. W. Kaiser, Z. Klimont, U. Lohmann, J. P. Schwarz, D. Shindell, T. Storelvmo, S. G. Warren, C. S. Zender, Bounding the role of black carbon in the climate system: A scientific assessment. *J. Geophys. Res. Atmos.* **118**, 5380–5552 (2013).
6. S. K. Akagi, R. J. Yokelson, C. Wiedinmyer, M. J. Alvarado, J. S. Reid, T. Karl, J. D. Crounse, P. O. Wennberg, Emission factors for open and domestic biomass burning for use in atmospheric models. *Atmos. Chem. Phys.* **11**, 4039–4072 (2011).
7. A. L. Hodshire, A. Akherati, M. J. Alvarado, B. Brown-Steiner, S. H. Jathar, J. L. Jimenez, S. M. Kreidenweis, C. R. Lonsdale, T. B. Onasch, A. M. Ortega, J. R. Pierce, Aging effects on biomass burning aerosol mass and composition: A critical review of field and laboratory studies. *Environ. Sci. Technol.* **53**, 10007–10022 (2019).
8. A. T. Ahern, E. S. Robinson, D. S. Tkacik, R. Saleh, L. E. Hatch, K. C. Barsanti, C. E. Stockwell, R. J. Yokelson, A. A. Presto, A. L. Robinson, R. C. Sullivan, N. M. Donahue, Production of secondary organic aerosol during aging of biomass burning smoke From fresh fuels and its relationship to VOC precursors. *JGR Atmospheres* **124**, 3583–3606 (2019).
9. T. Wang, K. Li, D. M. Bell, J. Zhang, T. Cui, M. Surdu, U. Baltensperger, J. G. Slowik, H. Lamkaddam, I. El Haddad, A. S. H. Prevot, Large contribution of in-cloud production of secondary organic aerosol from biomass burning emissions. *Npj Clim Atmos Sci* **7**, 149 (2024).
10. P. Lin, P. K. Aiona, Y. Li, M. Shiraiwa, J. Laskin, S. A. Nizkorodov, A. Laskin, Molecular characterization of brown carbon in biomass burning aerosol particles. *Environ. Sci. Technol.* **50**, 11815–11824 (2016).
11. Y. Rudich, N. M. Donahue, T. F. Mentel, Aging of organic aerosol: Bridging the gap between laboratory and field studies. *Annu. Rev. Phys. Chem.* **58**, 321–352 (2007).
12. G. Stefenelli, J. Jiang, A. Bertrand, E. A. Bruns, S. M. Pieber, U. Baltensperger, N. Marchand, S. Aksoyoglu, A. S. H. Prévôt, J. G. Slowik, I. El Haddad, Secondary organic aerosol formation from smoldering and flaming combustion of biomass: A box model parametrization based on volatility basis set. *Atmos. Chem. Phys.* **19**, 11461–11484 (2019).
13. B. B. Palm, Q. Peng, C. D. Fredrickson, B. H. Lee, L. A. Garofalo, M. A. Pothier, S. M. Kreidenweis, D. K. Farmer, R. P. Pokhrel, Y. Shen, S. M. Murphy, W. Permar, L. Hu, T. L. Campos, S. R. Hall, K. Ullmann, X. Zhang, F. Flocke, E. V. Fischer, J. A. Thornton, Quantification of organic aerosol and brown carbon evolution in fresh wildfire plumes. *Proc. Natl. Acad. Sci. U.S.A.* **117**, 29469–29477 (2020).
14. A. Akherati, Y. He, M. M. Coggon, A. R. Koss, A. L. Hodshire, K. Sekimoto, C. Warneke, J. De Gouw, L. Yee, J. H. Seinfeld, T. B. Onasch, S. C. Herndon, W. B. Knighton, C. D. Cappa, M. J. Kleeman, C. Y. Lim, J. H. Kroll, J. R. Pierce, S. H. Jathar, Oxygenated aromatic compounds are important precursors of secondary organic aerosol in biomass-burning emissions. *Environ. Sci. Technol.* **54**, 8568–8579 (2020).
15. M. K. Schueneman, D. A. Day, Z. Peng, D. Pagonis, O. J. Jenks, J. A. De Gouw, J. L. Jimenez, Secondary organic aerosol formation from the OH oxidation of phenol, catechol, styrene, furfural, and methyl furfural. *ACS Earth Space Chem.* **8**, 1179–1192 (2024).
16. B. Ervens, B. J. Turpin, R. J. Weber, Secondary organic aerosol formation in cloud droplets and aqueous particles (aqSOA): A review of laboratory, field and model studies. *Atmos. Chem. Phys.* **11**, 11069–11102 (2011).
17. K. E. Daumit, A. J. Carrasquillo, R. A. Sugrue, J. H. Kroll, Effects of condensed-phase oxidants on secondary organic aerosol formation. *J. Phys. Chem. A* **120**, 1386–1394 (2016).
18. A. Laskin, J. Laskin, S. A. Nizkorodov, Chemistry of atmospheric brown carbon. *Chem. Rev.* **115**, 4335–4382 (2015).
19. S. A. Mang, D. K. Henricksen, A. P. Bateman, M. P. S. Andersen, D. R. Blake, S. A. Nizkorodov, Contribution of carbonyl photochemistry to aging of atmospheric secondary organic aerosol. *J. Phys. Chem. A* **112**, 8337–8344 (2008).
20. S. A. Epstein, S. L. Blair, S. A. Nizkorodov, Direct photolysis of α-pinene ozonolysis secondary organic aerosol: Effect on particle mass and peroxide content. *Environ. Sci. Technol.* **48**, 11251–11258 (2014).
21. V. J. Baboomian, Y. Gu, S. A. Nizkorodov, Photodegradation of secondary organic aerosols by long-term exposure to solar actinic radiation. *ACS Earth Space Chem.* **4**, 1078–1089 (2020).
22. J. D. Smith, V. Sio, L. Yu, Q. Zhang, C. Anastasio, Secondary organic aerosol production from aqueous reactions of atmospheric phenols with an organic triplet excited state. *Environ. Sci. Technol.* **48**, 1049–1057 (2014).
23. Y. Chen, N. Li, X. Li, Y. Tao, S. Luo, Z. Zhao, S. Ma, H. Huang, Y. Chen, Z. Ye, X. Ge, Secondary organic aerosol formation from ^{3}C*-initiated oxidation of 4-ethylguaiacol in atmospheric aqueous-phase. *Sci. Total Environ.* **723**, 137953 (2020).
24. B. R. Go, Y. J. Li, D. D. Huang, C. K. Chan, Aqueous-phase photoreactions of mixed aromatic carbonyl photosensitizers yield more oxygenated, oxidized, and less light-absorbing secondary organic aerosol (SOA) than single systems. *Environ. Sci. Technol.* **58**, 7924–7936 (2024).
25. S. E. Paulson, P. J. Gallimore, X. M. Kuang, J. R. Chen, M. Kalberer, D. H. Gonzalez, A light-driven burst of hydroxyl radicals dominates oxidation chemistry in newly activated cloud droplets. *Sci. Adv.* **5**, eaav7689 (2019).
26. Y. Wang, H. Kim, S. E. Paulson, Hydrogen peroxide generation from α- and β-pinene and toluene secondary organic aerosols. *Atmos. Environ.* **45**, 3149–3156 (2011).
27. X. Chen, P. K. Hopke, W. P. L. Carter, Secondary organic aerosol from ozonolysis of biogenic volatile organic compounds: Chamber studies of particle and reactive oxygen species formation. *Environ. Sci. Technol.* **45**, 276–282 (2011).
28. W. Y. Tuet, Y. Chen, S. Fok, D. Gao, R. J. Weber, J. A. Champion, N. L. Ng, Chemical and cellular oxidant production induced by naphthalene secondary organic aerosol (SOA): Effect of redox-active metals and photochemical aging. *Sci. Rep.* **7**, 15157 (2017).
29. H. Tong, A. M. Arangio, P. S. J. Lakey, T. Berkemeier, F. Liu, C. J. Kampf, W. H. Brune, U. Pöschl, M. Shiraiwa, Hydroxyl radicals from secondary organic aerosol decomposition in water. *Atmos. Chem. Phys.* **16**, 1761–1771 (2016).
30. J. G. Charrier, C. Anastasio, Rates of hydroxyl radical production from transition metals and quinones in a surrogate lung fluid. *Environ. Sci. Technol.* **49**, 9317–9325 (2015).
31. K. M. Badali, S. Zhou, D. Aljawhary, M. Antiñolo, W. J. Chen, A. Lok, E. Mungall, J. P. S. Wong, R. Zhao, J. P. D. Abbatt, Formation of hydroxyl radicals from photolysis of secondary organic aerosol material. *Atmos. Chem. Phys.* **15**, 7831–7840 (2015).
32. L. Gerritz, J. Wei, T. Fang, C. Wong, A. L. Klodt, S. A. Nizkorodov, M. Shiraiwa, Reactive oxygen species formation and peroxide and carbonyl decomposition in aqueous photolysis of secondary organic aerosols. *Environ. Sci. Technol.* **58**, 4716–4726 (2024).
33. R. Kaur, J. R. Labins, S. S. Helbock, W. Jiang, K. J. Bein, Q. Zhang, C. Anastasio, Photooxidants from brown carbon and other chromophores in illuminated particle extracts. *Atmos. Chem. Phys.* **19**, 6579–6594 (2019).
34. A. Manfrin, S. A. Nizkorodov, K. T. Malecha, G. J. Getzinger, K. McNeill, N. Borduas-Dedekind, Reactive oxygen species production from secondary organic aerosols: The importance of singlet oxygen. *Environ. Sci. Technol.* **53**, 8553–8562 (2019).
35. P. Corral Arroyo, T. Bartels-Rausch, P. A. Alpert, S. Dumas, S. Perrier, C. George, M. Ammann, Particle-phase photosensitized radical production and aerosol aging. *Environ. Sci. Technol.* **52**, 7680–7688 (2018).
36. Z. Liang, L. Zhou, C. K. Chan, Fast generation of peroxides via atmospheric particulate photosensitization. *Sci. Adv.* **11**, eadr8776 (2025).
37. K. C. Edwards, A. L. Klodt, T. Galeazzo, M. Schervish, J. Wei, T. Fang, N. M. Donahue, B. Aumont, S. A. Nizkorodov, M. Shiraiwa, Effects of nitrogen oxides on the production of reactive oxygen species and environmentally persistent free radicals from α-pinene and naphthalene secondary organic aerosols. *J. Phys. Chem. A* **126**, 7361–7372 (2022).
38. L. Khachatryan, E. Vejerano, S. Lomnicki, B. Dellinger, Environmentally persistent free radicals (EPFRs). 1. Generation of reactive oxygen species in aqueous solutions. *Environ. Sci. Technol.* **45**, 8559–8566 (2011).
39. J. Wei, T. Fang, C. Wong, P. S. J. Lakey, S. A. Nizkorodov, M. Shiraiwa, Superoxide formation from aqueous reactions of biogenic secondary organic aerosols. *Environ. Sci. Technol.* **55**, 260–270 (2021).
40. J. Ma, J. Nie, H. Zhou, H. Wang, L. Lian, S. Yan, W. Song, Kinetic consideration of photochemical formation and decay of superoxide radical in dissolved organic matter solutions. *Environ. Sci. Technol.* **54**, 3199–3208 (2020).
41. L. Gerritz, V. Perraud, K. M. Weber, M. Shiraiwa, S. A. Nizkorodov, Application of UHPLC-ESI-MS/MS to identify free radicals via spin trapping with BMPO. *J. Phys. Chem. A* **128**, 10240–10249 (2024).
42. P. Ausloos, The photolysis of alkyl esters. *Can. J. Chem.* **36**, 383–392 (1958).
43. J. K. Royal, G. K. Rollefson, The photolysis of simple alkyl esters. *J. Am. Chem. Soc.* **63**, 1521–1525 (1941).
44. E. Bothe, M. N. Schuchmann, D. Schulte-Frohlinde, C. V. Sonntag, HO_2 elimination from α-hydroxyalkylperoxyl radicals in aqueous solution. *Photochem. Photobiol.* **28**, 639–643 (1978).
45. W. H. Park, A comprehensive review of pyrogallol: From fundamental chemistry to advanced applications and toxicological insights. *Biotech. Bioeng.* **123**, 527–543 (2025).
46. Z. Fang, A. Lai, D. Cai, R. Chunlin Li, J. Carmieli, X. Chen, Y. R. Wang, Secondary organic aerosol generated from biomass burning emitted phenolic compounds: Oxidative potential, reactive oxygen species, and cytotoxicity. *Environ. Sci. Technol.* **58**, 8194–8206 (2024).
47. H. Tong, P. S. J. Lakey, A. M. Arangio, J. Socorro, F. Shen, K. Lucas, W. H. Brune, U. Pöschl, M. Shiraiwa, Reactive oxygen species formed by secondary organic aerosols in water and surrogate lung fluid. *Environ. Sci. Technol.* **52**, 11642–11651 (2018).
48. C. Arellanes, S. E. Paulson, P. M. Fine, C. Sioutas, Exceeding of Henry's law by hydrogen peroxide associated with urban aerosols. *Environ. Sci. Technol.* **40**, 4859–4866 (2006).
49. K. McNeill, S. Canonica, Triplet state dissolved organic matter in aquatic photochemistry: Reaction mechanisms, substrate scope, and photophysical properties. *Environ. Sci. Processes Impacts* **18**, 1381–1399 (2016).
50. Y. Zhang, R. Del Vecchio, N. V. Blough, Investigating the mechanism of hydrogen peroxide photoproduction by humic substances. *Environ. Sci. Technol.* **46**, 11836–11843 (2012).
51. D. J. Lary, D. E. Shallcross, Central role of carbonyl compounds in atmospheric chemistry. *J. Geophys. Res.* **105**, 19771–19778 (2000).
52. T. Berkemeier, M. Ammann, U. K. Krieger, T. Peter, P. Spichtinger, U. Pöschl, M. Shiraiwa, A. J. Huisman, Technical note: Monte Carlo genetic algorithm (MCGA) for model analysis

of multiphase chemical kinetics to determine transport and reaction rate coefficients using multiple experimental data sets. *Atmos. Chem. Phys.* **17**, 8021–8029 (2017).
53. H. Sakugawa, I. R. Kaplan, W. Tsai, Y. Cohen, Atmospheric hydrogen peroxide. *Environ. Sci. Technol.* **24**, 1452–1462 (1990).
54. M. Fujii, E. Otani, Photochemical generation and decay kinetics of superoxide and hydrogen peroxide in the presence of standard humic and fulvic acids. *Water Res.* **123**, 642–654 (2017).
55. T. Arakaki, C. Anastasio, Y. Kuroki, H. Nakajima, K. Okada, Y. Kotani, D. Handa, S. Azechi, T. Kimura, A. Tsuhako, Y. Miyagi, A general scavenging rate constant for reaction of hydroxyl radical with organic carbon in atmospheric waters. *Environ. Sci. Technol.* **47**, 8196–8203 (2013).
56. M. C. Barth, B. Ervens, H. Herrmann, A. Tilgner, V. F. McNeill, W. G. Tsui, L. Deguillaume, N. Chaumerliac, A. Carlton, S. M. Lance, Box model intercomparison of cloud chemistry. *J. Geophys. Res. Atmos.* **126**, 10.1029/2021JD035486 (2021).
57. L. Ma, R. Worland, W. Jiang, C. Niedek, C. Guzman, K. J. Bein, Q. Zhang, C. Anastasio, Predicting photooxidant concentrations in aerosol liquid water based on laboratory extracts of ambient particles. *Atmos. Chem. Phys.* **23**, 8805–8821 (2023).
58. C. Anastasio, B. C. Faust, J. M. Allen, Aqueous phase photochemical formation of hydrogen peroxide in authentic cloud waters. *J. Geophys. Res.* **99**, 8231–8248 (1994).
59. M. O. Sunday, L. M. Dahler Heinlein, J. He, A. Moon, S. Kapur, T. Fang, K. C. Edwards, F. Guo, J. Dibb, J. H. Flynn Iii, B. Alexander, M. Shiraiwa, C. Anastasio, Hydrogen peroxide photoformation in particulate matter and its contribution to S(IV) oxidation during winter in Fairbanks, Alaska. *Atmos. Chem. Phys.* **25**, 5087–5100 (2025).
60. R. Kaur, C. Anastasio, Light absorption and the photoformation of hydroxyl radical and singlet oxygen in fog waters. *Atmos. Environ.* **164**, 387–397 (2017).
61. F. Leresche, J. R. Salazar, D. J. Pfotenhauer, M. P. Hannigan, B. J. Majestic, F. L. Rosario-Ortiz, Photochemical aging of atmospheric particulate matter in the aqueous phase. *Environ. Sci. Technol.* **55**, 13152–13163 (2021).
62. S. M. Griffith, R. F. Hansen, S. Dusanter, V. Michoud, J. B. Gilman, W. C. Kuster, P. R. Veres, M. Graus, J. A. De Gouw, J. Roberts, C. Young, R. Washenfelder, S. S. Brown, R. Thalman, E. Waxman, R. Volkamer, C. Tsai, J. Stutz, J. H. Flynn, N. Grossberg, B. Lefer, S. L. Alvarez, B. Rappenglueck, L. H. Mielke, H. D. Osthoff, P. S. Stevens, Measurements of hydroxyl and hydroperoxy radicals during CalNex-LA: Model comparisons and radical budgets. *J. Geophys. Res. Atmos.* **121**, 4211–4232 (2016).
63. P. Liu, C. Ye, C. Zhang, G. He, C. Xue, J. Liu, C. Liu, Y. Zhang, Y. Song, X. Li, X. Wang, J. Chen, H. He, H. Herrmann, Y. Mu, Photochemical aging of atmospheric fine particles as a potential source for gas-phase hydrogen peroxide. *Environ. Sci. Technol.* **55**, 15063–15071 (2021).
64. H. A. Al-Abadleh, S. A. Nizkorodov, Open questions on transition metals driving secondary thermal processes in atmospheric aerosols. *Commun. Chem.* **4**, 176 (2021).
65. L. M. D. Heinlein, J. He, M. O. Sunday, F. Guo, J. Campbell, A. Moon, S. Kapur, T. Fang, K. Edwards, M. Cesler-Maloney, A. J. Burns, J. Dibb, W. Simpson, M. Shiraiwa, B. Alexander, J. Mao, J. H. Flynn III, J. Stutz, C. Anastasio, Surprisingly robust photochemistry in subarctic particles during winter: Evidence from photooxidants. *Atmos. Chem. Phys.* **25**, 9561–9581 (2025).
66. W. Jiang, C. Niedek, C. Anastasio, Q. Zhang, Photoaging of phenolic secondary organic aerosol in the aqueous phase: Evolution of chemical and optical properties and effects of oxidants. *Atmos. Chem. Phys.* **23**, 7103–7120 (2023).
67. Z. Liang, L. Zhou, Y. Chang, Y. Qin, C. K. Chan, Biomass-burning organic aerosols as a pool of atmospheric reactive triplets to drive multiphase sulfate formation. *Proc. Natl. Acad. Sci. U.S.A.* **121**, e2416803121 (2024).
68. E. Harris, B. Sinha, D. Van Pinxteren, A. Tilgner, K. W. Fomba, J. Schneider, A. Roth, T. Gnauk, B. Fahlbusch, S. Mertes, T. Lee, J. Collett, S. Foley, S. Borrmann, P. Hoppe, H. Herrmann, Enhanced role of transition metal ion catalysis during in-cloud oxidation of SO_2. *Science* **340**, 727–730 (2013).
69. Y. Yan, T. Zhao, W. Huang, D. Fang, X. Zhang, L. Zhang, P. Huo, K. Xiao, Y. Zhang, Y. Zhang, The complexation between transition metals and water-soluble organic compounds (WSOC) and its effect on reactive oxygen species (ROS) formation. *Atmos. Environ.* **287**, 119247 (2022).
70. T. Finkel, N. J. Holbrook, Oxidants, oxidative stress and the biology of ageing. *Nature* **408**, 239–247 (2000).
71. J. P. S. Wong, M. Tsagkaraki, I. Tsiodra, N. Mihalopoulos, K. Violaki, M. Kanakidou, J. Sciare, A. Nenes, R. J. Weber, Effects of atmospheric processing on the oxidative potential of biomass burning organic aerosols. *Environ. Sci. Technol.* **53**, 6747–6756 (2019).
72. P. H. Chowdhury, Q. He, T. Lasitza Male, W. H. Brune, Y. Rudich, M. Pardo, Exposure of lung epithelial cells to photochemically aged secondary organic aerosol shows increased toxic effects. *Environ. Sci. Technol. Lett.* **5**, 424–430 (2018).
73. L. Gerritz, M. Schervish, P. S. J. Lakey, T. Oeij, J. Wei, S. A. Nizkorodov, M. Shiraiwa, Photoenhanced radical formation in aqueous mixtures of levoglucosan and benzoquinone: Implications to photochemical aging of biomass-burning organic aerosols. *J. Phys. Chem. A* **127**, 5209–5221 (2023).
74. R. Schmid, S. Heuckeroth, A. Korf, A. Smirnov, O. Myers, T. S. Dyrlund, R. Bushuiev, K. J. Murray, N. Hoffmann, M. Lu, A. Sarvepalli, Z. Zhang, M. Fleischauer, K. Dührkop, M. Wesner, S. J. Hoogstra, E. Rudt, O. Mokshyna, C. Brungs, K. Ponomarov, L. Mutabdžija, T. Damiani, C. J. Pudney, M. Earll, P. O. Helmer, T. R. Fallon, T. Schulze, A. Rivas-Ubach, A. Bilbao, H. Richter, L.-F. Nothias, M. Wang, M. Orešič, J.-K. Weng, S. Böcker, A. Jeibmann, H. Hayen, U. Karst, P. C. Dorrestein, D. Petras, X. Du, T. Pluskal, Integrative analysis of multimodal mass spectrometry data in MZmine 3. *Nat. Biotechnol.* **41**, 447–449 (2023).
75. J. Wei, T. Fang, P. S. J. Lakey, M. Shiraiwa, Iron-facilitated organic radical formation from secondary organic aerosols in surrogate lung fluid. *Environ. Sci. Technol.* **56**, 7234–7243 (2022).
76. R. Sander, Compilation of Henry's law constants (version 5.0.0) for water as solvent. *Atmos. Chem. Phys.* **23**, 10901–12440 (2023).
77. I. V. Perminova, F. H. Frimmel, A. V. Kudryavtsev, N. A. Kulikova, G. Abbt-Braun, S. Hesse, V. S. Petrosyan, Molecular weight characteristics of humic substances from different environments as determined by size exclusion chromatography and their statistical evaluation. *Environ. Sci. Technol.* **37**, 2477–2485 (2003).
78. D. K. Banerjee, C. C. Budke, Spectrophotometric determination of traces of peroxides in organic solvents. *Anal. Chem.* **36**, 792–796 (1964).
79. H. Keller-Rudek, G. K. Moortgat, R. Sander, R. Sörensen, The MPI-Mainz UV/VIS Spectral Atlas of gaseous molecules of atmospheric interest. *Earth Syst. Sci. Data* **5**, 365–373 (2013).
80. N. F. Christensen, R. Odai, K. H. Bates, H. G. Kjaergaard, Calculated absorption cross sections and photolysis rates of hydroperoxyaldehydes. *J. Phys. Chem. A* **130**, 111–120 (2026).
81. S. Hsieh, R. Vushe, Y. T. Tun, J. L. Vallejo, Trends in organic hydroperoxide photodissociation and absorption cross sections between 266 and 377 nm. *Chem. Phys. Lett.* **591**, 99–102 (2014).
82. H. Jiang, C. M. S. Ahmed, Z. Zhao, J. Y. Chen, H. Zhang, A. Canchola, Y.-H. Lin, Role of functional groups in reaction kinetics of dithiothreitol with secondary organic aerosols. *Environ. Pollut.* **263**, 114402 (2020).
83. R. Atkinson, J. Arey, Atmospheric degradation of volatile organic compounds. *Chem. Rev.* **103**, 4605–4638 (2003).
84. P. B. Shepson, E. O. Edney, E. W. Corse, Ring fragmentation reactions in the photooxidations of toluene and o-xylene. *J. Phys. Chem.* **88**, 4122–4126 (1984).
85. O. Garmash, M. P. Rissanen, I. Pullinen, S. Schmitt, O. Kausiala, R. Tillmann, D. Zhao, C. Percival, T. J. Bannan, M. Priestley, Å. M. Hallquist, E. Kleist, A. Kiendler-Scharr, M. Hallquist, T. Berndt, G. McFiggans, J. Wildt, T. F. Mentel, M. Ehn, Multi-generation OH oxidation as a source for highly oxygenated organic molecules from aromatics. *Atmos. Chem. Phys.* **20**, 515–537 (2020).
86. J. H. Seinfeld, S. N. Pandis, *Atmospheric Chemistry and Physics: From Air Pollution to Climate Change*, New York Academy of Sciences Series (John Wiley & Sons Inc., ed. 1, 2016).
87. M. Shiraiwa, U. Pöschl, Mass accommodation and gas–particle partitioning in secondary organic aerosols: Dependence on diffusivity, volatility, particle-phase reactions, and penetration depth. *Atmos. Chem. Phys.* **21**, 1565–1580 (2021).
88. B. Aumont, S. Szopa, S. Madronich, Modelling the evolution of organic carbon during its gas-phase tropospheric oxidation: Development of an explicit model based on a self generating approach. *Atmos. Chem. Phys.* **5**, 2497–2517 (2005).

Acknowledgments: We thank US National Science Foundation for the funding. We thank T. Berkemeier for sharing the code of MCGA. **Funding:** This work was funded by the US National Science Foundation (CHE-2203419; M.Sh. and S.A.N.) and the National Science Foundation Graduate Research Fellowship Program (L.G.). **Author contributions:** Conceptualization: L.G., S.A.N., and M.Sh. Methodology: L.G., M.Sc., P.S.J.L., S.A.N., and M.Sh. Investigation: L.G. Data curation: L.G. Resources: S.A.N. and M.Sh. Software: L.G., M.Sc., and P.S.J.L. Funding acquisition: L.G., S.A.N., and M.Sh. Supervision: S.A.N. and M.Sh. Project administration: M.Sh. Visualization: L.G., M.Sh. Validation: L.G. and P.L. Formal analysis: L.G. and P.S.J.L. Writing—original draft: L.G. and M.Sh. Writing—review and editing: L.G., M.Sc., P.S.J.L., S.A.N., and M.Sh. **Competing interests:** The authors declare that they have no competing interests. **Data, code, and materials availability:** All data and code needed to evaluate and reproduce the results in the paper are present in the paper and/or the Supplementary Materials. This study did not generate new materials.

Submitted 6 February 2026
Accepted 27 July 2026
Published 4 September 2026
10.1126/sciadv.aeg1621

ScienceAdvances

Superoxide formation upon photochemical aging of secondary organic aerosols derived from biomass burning precursors

Lena Gerritz, Meredith Schervish, Pascale S. J. Lakey, Sergey A. Nizkorodov, and Manabu Shiraiwa

Sci. Adv. **12** (36), eaeg1621. DOI: 10.1126/sciadv.aeg1621

Science Advances (ISSN 2375-2548) is published by the American Association for the Advancement of Science. 1200 New York Avenue NW, Washington, DC 20005. The title *Science Advances* is a registered trademark of AAAS.